



RFID+: Spatially Controllable Identification of UHF RFIDs via Controlled Magnetic Fields

Donghui Dai, *The Hong Kong Polytechnic University*; Zhenlin An, *The Hong Kong Polytechnic University and Princeton University*; Zheng Gong, *The Hong Kong Polytechnic University*; Qingrui Pan, *The Hong Kong Polytechnic University and The University of Edinburgh*; Lei Yang, *Shenzhen Research Institute, The Hong Kong Polytechnic University*

<https://www.usenix.org/conference/nsdi24/presentation/dai>

This paper is included in the
Proceedings of the 21st USENIX Symposium on
Networked Systems Design and Implementation.

April 16–18, 2024 • Santa Clara, CA, USA

978-1-939133-39-7

Open access to the Proceedings of the
21st USENIX Symposium on Networked
Systems Design and Implementation
is sponsored by



RFID+: Spatially Controllable Identification of UHF RFIDs via Controlled Magnetic Fields

Donghui Dai¹, Zhenlin An^{1,2}, Zheng Gong¹, Qingrui Pan^{1,3}, Lei Yang^{1,4}

¹The Hong Kong Polytechnic University, ²Princeton University, ³The University of Edinburgh

⁴Shenzhen Research Institute, The Hong Kong Polytechnic University

Abstract

In the fast-paced landscape of UHF RFID technology, achieving precise spatial-selective identification is of critical importance in the logistics and retail domain. This work introduces RFID+, a magnetically-driven UHF RFID system that leverages the matching loops of commercial-off-the-shelf UHF RFID tags for efficient energy harvesting from tailored magnetic fields. The RFID+ delivers a level of spatial precision comparable to that of HF NFC systems, effectively mitigating issues of miss-reading and cross-reading. Our primary contributions reside in the development of a specialized multi-turn, capacitor-segmented coil antenna and an innovative fast inventory algorithm. The RFID+ seamlessly integrates traditional radiative coupling with the innovative magnetic coupling in UHF RFID systems, bolstering their overall performance and efficiency. Real-world pilot studies in warehouses and logistics settings reveal that RFID+ significantly diminishes the miss-reading rate from 22.9% down to a remarkable 1.06%, while entirely eliminating cross-reading challenges. Moreover, our RFID+ variant demonstrates better resilience against materials traditionally challenging for UHF RFID, such as water bottles and containers. These advancements make RFID+ exceedingly relevant for practical applications in logistical networks.

1 Introduction

Ultra-high frequency (UHF) Radio-Frequency Identification (RFID) has arisen as a transformative non-contact identification paradigm in the logistics and retail domains [1–3]. By harnessing wireless radio frequency (RF) communication, RFID infrastructures can effortlessly access unique Electronic Product Codes (EPC) from passive RFID tags affixed to various items. A key criterion is the pinpoint identification of tagged objects within a predetermined Region of Interest (ROI). For instance, in automated shopping arenas, RFID systems discern customer selections within a specified vicinity near the departure point, commonly termed the checkout zone; in environments such as airports or manufacturing units, RFID systems adeptly oversee an array of items transitioning on conveyors; within warehouse contexts, RFID systems diligently oversee item dynamics at ingress and egress junctures. The efficacy of the RFID paradigm hinges on its prowess to execute these operations expeditiously and with unparalleled accuracy, even amidst challenging operational conditions.

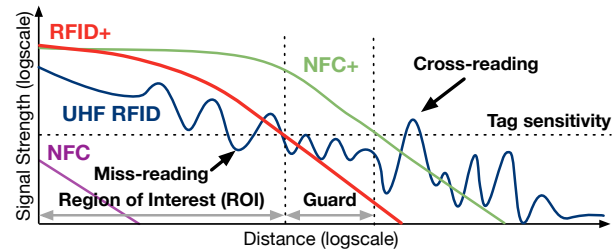


Fig. 1: The unpredictable propagation behavior of RF signals has traditionally rendered UHF RFID susceptible to anomalies of miss-reading and cross-reading. RFID+ defies this norm by introducing a controlled magnetic field, effectively addressing both miss-reading and cross-reading challenges similar to the HF NFC+.

Nevertheless, without fully realizing the extensive capabilities of RFID, present-day RFID systems remain under the shadow of two significant challenges: *miss-reading anomaly* and *cross-reading anomaly*. Conventionally, UHF RFID tags operate in far-field domains, where the RF signal propagates as planar electromagnetic (EM) waves, decaying at a pace of $O(1/r^2)$ in relation to distance r . As depicted in Fig. 1, governing the far-field RF signals is intricate due to their multifaceted interplay with RF-inimical materials such as metals or liquids. These signals are prone to reflection or absorption. Particularly, within the ROI, there is the potential for multipath signals to nullify each other, culminating in "blind zones" where the RF intensity is not sufficient to trigger relevant RFID tags (i.e., the miss-reading anomaly). In contrast, outside the designated ROI, multipath signals may combine constructively, inadvertently leading to the recognition of undesired tags (i.e., the cross-reading anomaly). For instance, as illustrated in Fig. 2(a-b), the confined and crowded nature of the checkout lane in an automated store inherently leads to unavoidable tag miss-reading and cross-reading anomalies.

Modern RFID systems face challenges in addressing cross-reading and miss-reading anomalies [4, 5] simultaneously. While increasing transmission power and sensitivity can improve detection, it often leads to unintended cross-readings. On the other hand, mitigating cross-reading can cause missed detections. Although recent debates favor a localization-based approach over the traditional binary reading, its effectiveness is questioned due to challenges like the "garbage in, garbage out" [6, 7]. While RFGo [8] leverages machine learning for enhanced detection, it falls short in dynamic scenarios. NFC+ [7] previously explored the potential of long-range, magnetic-coupling HF NFC at 13.56MHz as an alternative to UHF RFID for improved ROI management. Magnetic signals inherently minimize cross-reading owing to their rapid decay,

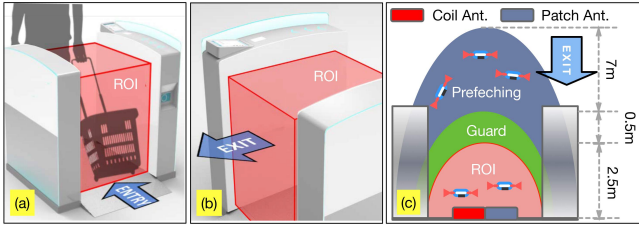


Fig. 2: Checkout lane. (a) and (b) show the entrance and the exit of the lane. These two figures are reproduced from [8]. (c) shows our prefetching augmented ROI coverage.

and diminish the likelihood of miss-reading because of their pronounced penetration through challenging materials such as liquids and metals. However, NFC+ still faces three challenges: (1) HF tags are substantially more expensive than UHF tags, posing deployment barriers; (2) existing infrastructures, heavily reliant on UHF RFIDs [9], face challenges in adopting NFC due to compatibility issues; (3) NFC's reading rate of 50 tags/s is dwarfed by RFID's 200 tags/s, making NFC less suitable for high-speed inventory tasks such as those involving moving tags on conveyors or checkout zones.

Contrary to HF NFC tags that use *coil antennas* for inductive or magnetic coupling, UHF RFID tags commonly utilize *dipole antennas* to capture and emit electromagnetic waves. The absence of coils may give the *misleading impression that UHF RFID tags are ill-suited for energy harvesting from magnetic fields*. However, as illustrated in Fig. 24 (Appendix A), the architecture of a standard UHF RFID tag includes a small loop (highlighted in blue) situated near the chip. Commonly referred to as the "matching" or "tuning" loop, this component is critical in optimizing energy harvesting and offering protection against over-voltage issues. Our findings indicate that this inherent loop structure can, in fact, enable UHF RFID tags to harvest energy from magnetic fields, thereby mimicking the inductive coupling characteristics as seen in HF NFC.

In this work, we introduce RFID+, a magnetically-driven UHF RFID system that innovatively repurposes the matching loop of a UHF RFID tag as an RF frontend for both energy harvesting and communication. The system's objective is the spatially selective identification of UHF RFIDs through precision-controlled magnetic fields. As depicted in Fig. 1, RFID+ not only emulates the propagation features of NFC+ but also overcomes its limitations. Specifically, RFID+ effectively interfaces with widely-used, economical UHF RFIDs while maintaining a high reading rate.

However, translating RFID+ into practice poses three significant engineering hurdles:

- Initially, the feasibility of harnessing energy from magnetic fields through the matching loops of commercial UHF RFIDs has not been thoroughly investigated. To fill this research void, we conduct an exhaustive feasibility study that shines light on the underlying principles of magnetically-driven UHF RFID systems. Through empirical evaluations conducted in real-world scenarios, we not only establish the viability of this technique but also substantiate its effectiveness and broad applicability.

- Secondly, the necessity arises for the integration of a coil antenna into a UHF RFID reader, enabling the creation of a controllable magnetic field. Traditional wavelength-matched loop antennas (single-coil) commonly seen in HF NFC (i.e., 13.56 MHz) become problematic when shifted to the UHF band (i.e., 860 – 960 MHz). This difficulty stems from the notably shorter wavelength at UHF relative to the loop's circumference, potentially leading to certain regions experiencing mutual magnetic field nullification. To address this concern, we put forward a tailored multi-turn, capacitor-segmented coil antenna complemented by a high-impedance reflector, striving for an even and directional magnetic field distribution.
- Thirdly, RFID systems driven by magnetic fields have a range that caps at about 3m, substantially less than the potential 10m span of those powered by radiative methods, largely attributed to the swift dissipation of magnetic fields. This confined ROI intensifies the need for prompt tag reading. To mitigate potential delays, especially with fast-moving tags, we initially engage a conventional far-field, radiatively-coupled reader to prefetch potential tags moving toward the ROI. Subsequently, we incorporate Bloom filters alongside the near-field, magnetically-coupled reader to streamline the inventory procedure.

Contributions. This study re-examines the intricate ROI management in UHF RFID through the lens of inductive coupling. We present three major contributions: 1) We validate the potential of magnetically-driven UHF RFID; 2) We introduce innovative coil antenna designs and a tailored inventory algorithm for RFID+; 3) Through rigorous tests and real-world pilots, we demonstrate RFID+'s efficacy. We hope that this research revitalizes academic discourse surrounding magnetically-driven UHF RFID systems in typical scenarios.

2 Magnetically-Driven UHF RFID

In this section, we start by exploring the basics of UHF RFID, introduce inductive coupling via tags' matching loops, and finally assess the feasibility across COTS UHF tags.

2.1 Background

The coupling mechanism describes the means by which systems engage in the interchange of energy or information. The mechanisms adopted by HF NFC and UHF RFID vary significantly, largely owing to the different frequency ranges in which these systems operate.

- **Inductively-Coupled HF NFC:** Operating at 13.56MHz, HF NFC employs inductive coupling facilitated by coil antennas. In this arrangement, an oscillating electrical current flows through the reader's coil, generating a variable magnetic field in the surrounding area. When an NFC tag comes within this field's sphere of influence, the magnetic flux induces a current in the tag's coil antenna, thereby activating the NFC chip and initiating communication with the reader. Given the reactive

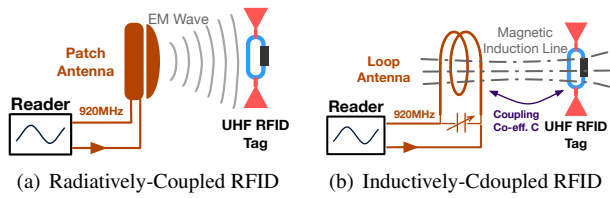


Fig. 3: Rationale behind Magnetically-driven UHF RFID

nature of these fields, the effective communication range is generally limited to a short span of several centimeters.

- **Radiatively-Coupled UHF RFID:** Typically operating within the 860-960 MHz frequency range, UHF RFID utilizes radiative coupling, commonly executed through dipole antennas. In this scenario, the reader emits a UHF radio wave that, upon reaching an RFID tag, induces an electric current in the tag's antenna. Utilizing backscatter technology, the tag then modifies and reflects the wave back to the reader. This method allows for a substantially extended operational range, often reaching up to several meters.

In essence, while HF NFC primarily employs inductive coupling for close-proximity interactions, UHF RFID leverages radiative coupling to enable longer-distance engagements.

2.2 Inductive Coupling via Matching Loops

Inductive coupling usually requires coil-configured antennas that the UHF RFID tags are short of. Thus, it seems that UHF RFID tags are not reactive to magnetic fields at first glance. Actually, as illustrated in Fig. 25 (Appendix A), every RFID tag inherently incorporates a single-turn coil, referred to as the matching loop. This essential component bridges the gap between dipole-style antennas and the tag's integrated chips (ICs), serving three primary functions: Firstly, it facilitates impedance matching between the antenna and the chip, ensuring optimal power conveyance. Secondly, this loop aids in adjusting the voltage levels to align with the chip's requisites. Lastly, by safeguarding the correct impedance and voltage calibrations, it inadvertently fortifies the RFID chip against potential over-voltage detriments.

These loops can essentially act as standalone coil antennas. When exposed to a magnetic field, these loops capture an induced electrical current that then flows to energize the chip, successfully accomplishing inductive coupling. Therefore, it becomes feasible to power and interface with UHF RFID tags through magnetic fields, akin to the operation seen in NFC systems. To elucidate further, let us juxtapose the operational mechanics of conventional radiatively-coupled RFID systems with those of our innovative magnetically-coupled ones. Fig.3(a) portrays the conventional system where the reader is equipped with a patch antenna – a specific variation of a dipole antenna. A tag derives its power from the transmitted electromagnetic waves fully using its own dipole antenna. On the other hand, Fig.3(b) illustrates our approach: the reader comes outfitted with a coil antenna, purposed for the generation of concentrated magnetic fields. This magnetic flux subsequently traverses the tag's matching loop, thereby

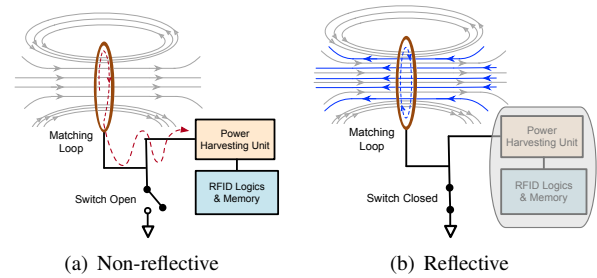


Fig. 4: Magnetic backscatter communication. (a) With the switch is open, the induced current is directed towards the harvesting unit; (b) With the switch is closed, the coil experiences a short-circuit. The current generated within the coil fosters an opposing magnetic field, which subsequently resonates with the reader's coil, acting as a reflection.

inducing an electric current. The distinction between the two approaches lies solely in their signal propagation mechanisms – via either a patch or a coil antenna. All other system parameters, including the operating frequency and transmission power, remain unaltered, making this a financially judicious solution.

2.3 Communication Immutability

A concern may arise regarding the necessity of altering communication protocols when passive tags obtain power through magnetic fields. This concern can be addressed by examining the two communication links of UHF RFID: the downlink and the uplink.

- **Downlink (Reader \Rightarrow Tag):** In the downlink, where the reader communicates to the tag, the goal is to query tags or send specific commands. The reader employs an Amplitude Shift Keying (ASK) method, encoding different bit values with varying amplitude levels. This ASK causes magnetic strength changes, inducing a current with amplitude variation in the tag's matching loop. Thus, even with magnetic power derivation, the tag's chip can decode ASK commands.

- **Uplink (Tag \Rightarrow Reader):** In the uplink, where tags communicate to the reader, the primary goal is to send the stored EPC. When energized by the reader's signal, passive tags use "backscatter modulation" to transmit data. This process involves a switch that connects the tag's peripherals to its IC, as depicted in Fig. 4. When the switch is on, the tag directs the induced current from the loop to the chip, making it absorbent and non-reflective. However, when off, the tag grounds the chip, and the loop-initiated current, following Lenz's law, creates an opposing magnetic field. This renders the RFID tag reflective, sending the loop-induced power back to the reader. The tag thus communicates bits by toggling between its reflective and non-reflective states or backscattering.

Thus, the modulation techniques employed for both downlink and uplink communication remain unmodified.

2.4 Experimental Verification

We verify the feasibility of the magnetically-driven approach using standard COTS RFID hardware. Fig. 5 provides a visual representation of the experimental configuration, showcasing the tags evaluated. We utilized a widely-used commercial RFID reader (Impinj R420 [10]) set to a frequency of

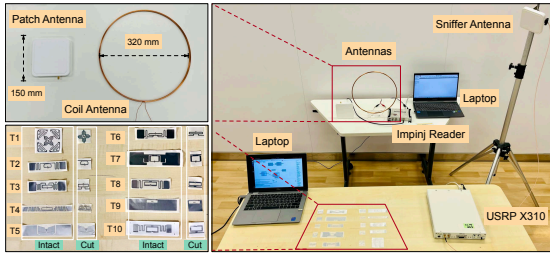


Fig. 5: Experiment Validation. A commercial Impinj reader is equipped with a patch antenna and a coil antenna, respectively. Ten types of commercial tags are tested.

920MHz. Alongside this, we deployed the USRP X310 [11] device as a dedicated sniffer to capture the communication between the reader and the tag. Our tests incorporated two distinct reader antennas: a $15 \times 15 \text{ cm}^2$ patch antenna and a coil antenna with a 32cm diameter. The reader is alternately connected to each of these antennas, with the transmission power maintained at 30dBm. The sniffer was strategically placed close to the reader antenna, roughly 30cm away. For each trial, we arranged each tag in an approximately parallel orientation to the loop to maximize the capture of magnetic flux.

Comparative Tests on Loop Role. Fig. 26 has validated that COTS RFID tags can be activated and queried using magnetic fields while the communication protocol remains consistent¹. To test if tags can continue to harness energy from magnetic fields using only matching loops, we conducted two comparative inventory tests with an M4 tag (i.e., T1) positioned 50cm away. We alternated between using a patch and coil antenna for the reader. The first test assessed the RN16 responses of the unaltered tag. The signals from both antennas were largely consistent, as seen in Fig. 6(a) and (b). In the second test, after cutting off the tag's dipole antenna and leaving only the matching loop (see Fig. 5), the tag was unresponsive to EM-waves but still functions effectively when exposed to magnetic fields, as shown in Fig. 6(c) and (d). The comparative results emphasize the crucial role of the matching loop in energy harvesting. The comparative analyses were also conducted for the other nine tag types (T2-T10, as depicted in Fig. 5). The outcomes were consistent across all tests as summarized in Table 2.

3 Overview

At a high level, RFID+ is elegantly simple: We strategically replace the conventional electric patch antennas of UHF RFID readers with tailored coil antennas, in the pursuit of precisely controlled magnetic field emission aimed at UHF RFID tags within a specified ROI. Benefiting from rapid attenuation and strong penetration capabilities, magnetically-driven RFID+ minimizes miss-reading and cross-reading anomalies. To this end, we introduce a unique multi-turn, capacitor-segmented coil design for our UHF RFID system in §4 and devise a

¹More details can be found in Appendix A.

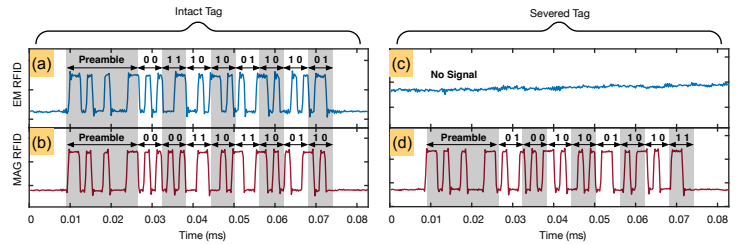


Fig. 6: Captured RN16 signals from a tag across four distinct conditions. (a) and (b) display signals procured from the unaltered tag, powered by EM waves and magnetic fields, correspondingly. (c) and (d) illustrates signals from the modified tag whose dipole antenna is cut off. As a result, it is unresponsive to EM-wave query anymore but still functions effectively when exposed to magnetic fields.

prefetching-based algorithm to speed up readings in §5. The subsequent sections elaborate on the technical details.

Scope. The matching loops inherent in existing UHF RFID tags are clearly not optimized for energy extraction from magnetic fields, resulting in low radiation efficiency and a relatively limited range. Our approach balances compatibility with controllability, designed to integrate seamlessly with existing UHF RFID tags while offering precise ROI management in near-field settings like conveyor belts or check-out zones. In such environments, the desired operational range is approximately 100-200cm, consistent with prior findings [7, 8, 12]. Thus, our intent is not to supplant existing radiatively-coupled UHF RFID systems or to extend the long-range reading capability, but rather to complement them by offering improved spatial controllability within confined ROIs.

4 Spreading Magnetic Fields

In this section, we delve into the novel coil antenna design tailored for our magnetically-driven UHF RFID system.

4.1 Necessity of a Novel Coil Antenna

Why are traditional coil antennas inadequate for the specific requirements of magnetically-driven UHF RFID systems? To answer this question, we use ANSYS HFSS [13] software to simulate the distributions of magnetic fields generated by a 7.5cm radius single-turn coil at both 13.56MHz (HF NFC norm) and 920MHz (UHF RFID standard). The findings, illustrated in Fig. 7(a), reveal a uniform magnetic field distribution at the 13.56MHz frequency. However, at 920MHz, the field distribution shown in Fig. 7(b) exhibits irregularities, including four intensified regions surrounding the loop and five weaker areas, or "blind zones," both centrally and at the corners. Such uneven distribution highlights the limitations of conventional coil antennas for UHF RFID applications, specifically in terms of potential activation failures in these blind zones.

The observed unevenness can be explained as follows: the coil is considered as a composition of countless tiny elements, each generating its unique magnetic field with an initial phase. The overall field is the sum of these individual fields. Phase alignment results in constructive field addition, while misalignment can cause mutual nullification. To better visualize

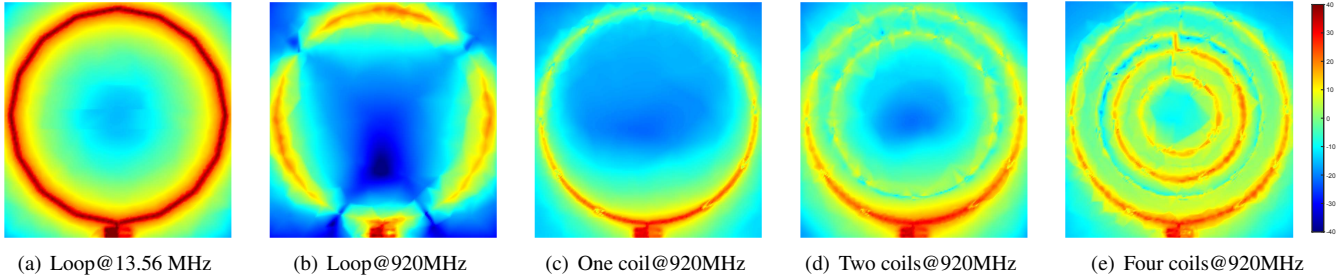


Fig. 7: Simulated magnetic intensity in the vicinity of five distinct antenna structures. (a) denotes an unsegmented loop actuated by a 13.56 MHz HF excitation signal; (b) illustrates an unsegmented loop energized by a 920 MHz UHF signal; (c) offers a depiction of a segmented loop equipped with lumped capacitors, resonating to a 920 MHz UHF signal; (d) presents a two-turn segmented loop integrated with fork capacitors, subjected to a 920 MHz UHF excitation; and (e) displays a multi-turn segmented spiral loop with fork capacitors, stimulated by a 920 MHz UHF signal.

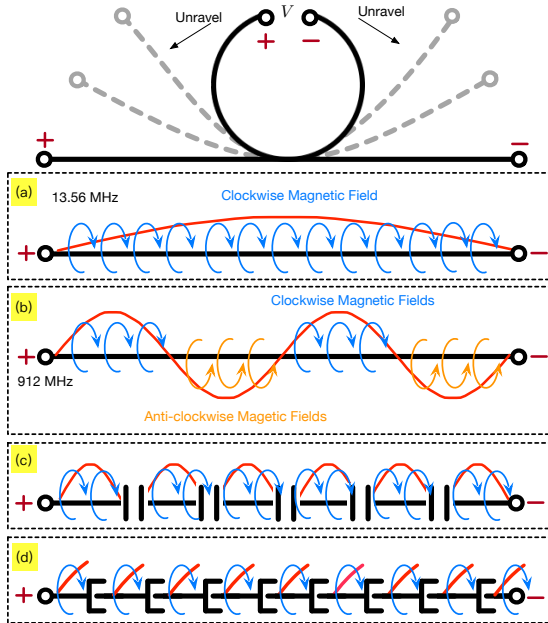


Fig. 8: Analysis on a loop antenna. (a) Magnetic fields remain in consistent directions at 13.56MHz; (b) The magnetic fields change their directions alternatively along the coil. (c) The capacitor-segmented coil eliminates the disparities in the initial phase. (d) The microstrip lumped capacitor-segmented coil.

the phase variations as the signal traverses the coil, we represent the loop linearly, depicted in Fig. 8. With HF signals, characterized by a 22-meter wavelength, phase discrepancies across coil elements are negligible due to the significant disparity between the wavelength and the coil's 50 cm circumference. A maximum phase difference is just 0.14 radians, ensuring a predominantly in-phase superposition, as displayed in Fig. 8(a). Conversely, the UHF signal has a wavelength of 32 cm, comparable to the coil's circumference. As the signal traverses the coil, it completes about two cycles, as depicted in Fig. 8(b). This causes each element's initial phase to fluctuate between 0 and 2π repeatedly. The clockwise magnetic fields stem from positive currents, while negative currents yield anti-clockwise ones. When refashioned into a loop, these opposing magnetic fields combine out-of-phase, resulting in the observed uneven distribution. Thus, there arises a pressing demand to pioneer a novel coil antenna design tailored for the proposed magnetically-driven UHF RFID systems.

4.2 Capacitor-Segmented Coil Antenna

The loop antenna's limitation stems from the incoherent amalgamation of different elements because of phase discrepancies. A straightforward remedy might be to shrink the loop's size to $1/4$ wavelength, ensuring better phase alignment. Yet, antenna theory fundamentals suggest that a loop antenna resonates (evident as a purely real impedance) only when its circumference is roughly equal to a wavelength [14]. More accurate dimensions need to be ascertained through specialized 3D electromagnetic simulation.

Capacitor-Segmented Loop. To counteract the loop antenna's limitations, we propose segmenting the loop physically and inserting capacitors between adjacent segments, as shown in Fig. 8(c). Each segment can then be modeled as an equivalent RLC circuit. Let R , L and C represent the intrinsic resistance and inductance of a segment, and the capacitance respectively. Capacitors are known to resist sudden voltage changes. Under AC conditions, the current behind a capacitor obtains a phase shift ϕ , which is given by:

$$\phi = \arctan \left(\frac{2\pi fL - \frac{1}{2\pi fC}}{R} \right) \quad (1)$$

where f symbolizes the frequency of the signal. This equation indicates that by fine-tuning the capacitor's value, one can methodically counterbalance a desired phase shift. As shown in Fig. 8(c), segmentation at intervals of half a wavelength along the line results in a 180° phase change each time. By strategically selecting the capacitance values, a corrective phase shift of -180° is introduced by each capacitor. This ensures the RF signal flowing between consecutive capacitors retains a uniform initial phase shift. Such alignment gives rise to uniform clockwise magnetic fields across segments. When the linear arrangement is formed into a loop, this coherence is maintained, yielding a consistent magnetic field distribution. This technique can uphold the loop's size while guaranteeing a balanced field distribution.

Fork-Shaped Lumped Capacitor. Utilizing a single discrete capacitor is straightforward, but integrating several capacitors onto a PCB might result in unexpected power consumption and enlarged dimensions. Contemporary antenna systems lean towards microstrip lumped antennas that

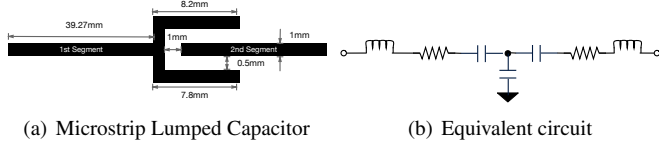


Fig. 9: Fork-shaped Lumped Capacitor. (a) shows the structure and the size of the lumped capacitor. (b) shows the equivalent circuit.

smartly embed lumped components within the antenna's design. Inspired by prior designs in microstrip antennas [15–17], we adopt the fork-shaped lumped capacitors. As shown in Fig. 9(a), the capacitor is implemented by the microstrip line. In the figure, two segments are positioned 1mm apart. The former segment ends with a three-sided forked shape that interfaces with the beginning of the subsequent segment. Specifically, the dimensions of the top, left, and bottom sides are 8.2mm, 4mm, and 7.8mm, respectively. The bottom side is slightly shortened compared to the top to fit the arc design. Fig. 9(b) presents the equivalent circuit where the three sides are modeled as individual capacitors.

The capacitance of the lumped capacitor is approximated by $8\epsilon\sqrt{A/\pi}$, where A represents the area of the forked configuration and ϵ is the permittivity coefficient. This equation suggests that a considerable area is needed to achieve a substantial capacitance and the corresponding large phase shift. Thus, to avoid bulky capacitors, we trim the segment length, thereby adjusting the required phase. Each segment, featuring the aforementioned fork-shaped capacitor, was iteratively determined in HFSS by tuning the phase shifts according to segment length. Specifically, our design sets the segment length at 3.927cm, roughly 11.9% of the 32.872cm wavelength, deviating from the standard half-wavelength model. It is crucial to note the compromise: this design necessitates four times as many lumped capacitors than its half-wavelength counterpart. Fig. 8(d) showcases this coil design. As the signal traverses a 3.927cm segment, its phase shifts by 42.84° . The lumped capacitor then counters this shift by -42.84° , ensuring consistent signal alignment across segments.

4.3 Spiral Coil Antenna

As illustrated in Fig. 7(c), the capacitor-segmented loop offers a markedly even distribution of magnetic field intensity compared to the conventional loop design. The updated design spreads this energy more uniformly. However, a region of diminished intensity remains near the center. This drawback can be remedied by using multi-turn coils. Accordingly, we introduce a spiral coil antenna, whose design and implementations are shown in Fig. 10. This design features four distinct coil turns, artfully arranged in a spiral layout, with both the start and end points of the coil connected using via-holes. A greater coil density might seem beneficial but poses a challenge: the potential coupling between neighboring coils. To alleviate this potential interference, we reserve an 18mm spacing between them (i.e., half of the segment length) after iterative optimization. The simulated magnetic intensity distribution of two-turn and four-turn coil antenna are shown in Fig. 7(d) and

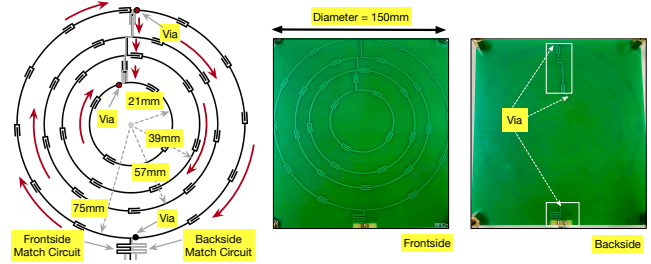


Fig. 10: Spiral Coil Antenna. Multi-turns of coils are arranged in a spiral fashion.

(e), respectively. The simulation results reinforce our hypothesis that a spiral configuration not only enhances the effective electrical length of the loop antenna but also accentuates its intensity with the addition of more turns.

4.4 Directional Coil Antenna

Many applications, like inventory management, require directional coverage to meet user expectations. It is also notable that today's EM-driven UHF RFID systems use directional patch antennas. Thus, aligning with industry norms, our next steps will focus on crafting a directional coil antenna. A conventional solution is to place a metal reflector behind the coil antenna to direct magnetic fields forward. However, this approach faces the issue of half-wave loss. When RF signals transition from low to high impedance boundaries, the reflected wave undergoes a 180° phase shift. As depicted in Fig. 11(a), if the coil-reflector gap is $< \lambda/4$, these shifted magnetic fields destructively interfere with those from the opposite side. The constructive superpositions occur only when the gap is set to $\lambda/4$. For our 32cm wavelength, a separation of about 8cm is required, increasing antenna thickness.

Mushroom-like HIS. Inspired by the artificial magnetic conductors [18], we introduce a high-impedance surface (HIS) approach to intrinsically mitigate the half-wave loss. The core principle behind HIS is illustrated in Fig. 11(b) and (c). Resting atop a metallic base, a series of compact square patches are arranged in a grid pattern. These mushroom-like patches (called HIS elements) connect to the base via central via-holes, with a deliberate spacing between them. As a result, adjacent elements essentially function as capacitors, connected through the via-hole to the base metal below. Given the inherent parasitic resistance, two proximate HIS elements together resemble a standard parallel resonant RL circuit. The impedance related to an HIS can be expressed as:

$$Z_{\text{HIS}} = \frac{j\omega L}{1 - \omega^2 LC} = \frac{j\omega L}{1 - (\omega/\hat{\omega})^2} \quad (2)$$

where ω signifies the angular frequency of the prevailing magnetic field, while $\hat{\omega} = 1/\sqrt{LC}$ represents the resonant angular frequency. The L and C refer to the parasitic resistance and lumped capacitance, respectively. Their values are calculated as outlined in [19]:

$$L = \frac{\eta_s}{\omega} \tan(\beta h) \text{ and } C = \frac{1}{\pi} w \epsilon_0 (\epsilon_{r1} + \epsilon_{r2}) \cosh^{-1} \left(\frac{D}{g} \right) \quad (3)$$

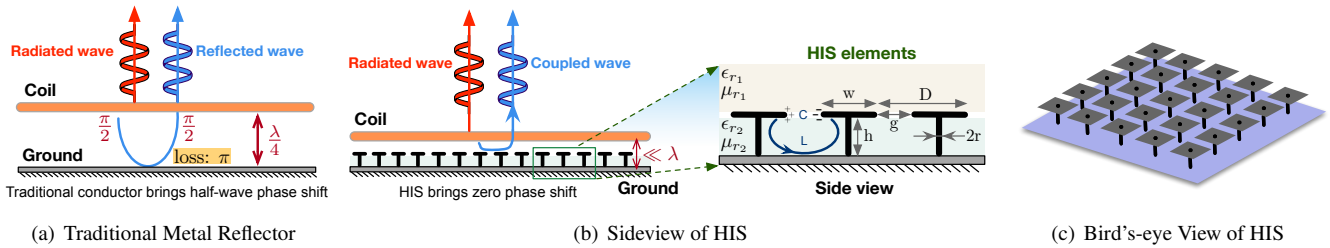


Fig. 11: Reflection-Induced Phase Shift. (a) When magnetic signals encounter a metallic ground, they experience a 180° phase shift due to half-wave loss. To counterbalance this phase shift, the separation between the coil and the ground must be set to $\lambda/4$. If the gap is less than $\lambda/4$, reflected signals will destructively interfere with the upward-propagating magnetic waves. (b) Illustrates a side view of the mushroom-structured HIS, designed to minimize the phase shift from reflections, effectively bringing it close to zero. (c) Depicts a top-down or bird's-eye view of the HIS.

Here, $\eta_s = \sqrt{\mu_0 \mu_{r2} / \epsilon_0 \epsilon_{r2}}$ and $\beta = \omega \sqrt{\mu_0 \mu_{r2} \epsilon_0 \epsilon_{r2}}$ stand for the intrinsic wave impedance and propagation constant, respectively. The constants ϵ_0 and μ_0 are the permittivity and permeability of a vacuum, with relevant parameters defined in Fig. 11(b). By varying the size and spacing of these elements, one can fine-tune the resonant frequency and achieve the desired impedance characteristics for specific applications.

Zero-Phase Shift. When the HIS's resonant frequency $\hat{\omega}$ aligns with the frequency ω of the impinging magnetic field, the HIS manifests as an "infinite" impedance surface, as evident from Eqn. 2. This phenomenon arises because the equation's denominator approaches zero. In this scenario, the magnetic field's reflected phase by the HIS is articulated by

$$\theta = \text{Im} \left(\ln \left(\frac{Z_{\text{HIS}} - \eta_0}{Z_{\text{HIS}} + \eta_0} \right) \right) \approx 0 \quad (4)$$

because $Z_{\text{HIS}} \gg \eta_0$. This implies that an HIS can proficiently eliminate the 180° phase shift induced by the half-wave loss, facilitating constructive coupling of the reflected waves via the HIS. By leveraging the properties of the HIS, it becomes possible to significantly reduce the required separation between the HIS and the coil antenna to well below $\lambda/4$. Simultaneously, nearly all of the magnetic energy is constructively redirected to the opposing side of the antenna. The simulated magnetic field distributions with and without an HIS reflector are compared in Appendix B.

4.5 Coil Antenna Array

In near-field communications, interactions are primarily driven by magnetic fields, which are divided into reactive and radiative near-field domains. The reactive near-field resides close to the antenna, typically within $0.62 \sqrt{D^3 / \lambda}$, while the radiative near-field or Fresnel Region extends to about $2D^2 / \lambda$, with D representing the antenna's maximum linear dimension (i.e., aperture). For optimal performance, our single coil's outermost circumference is set to λ , making its diameter $D = \lambda / \pi$. Theoretically, the near-field range of a single-turn coil antenna becomes approximately 12cm, which falls short for many practical applications. Despite incremental advancements from components such as capacitor-segmented, multi-turn coils, and the zero-phase reflection of HISs, the range expansion is still insufficient, extending to merely 50cm. To

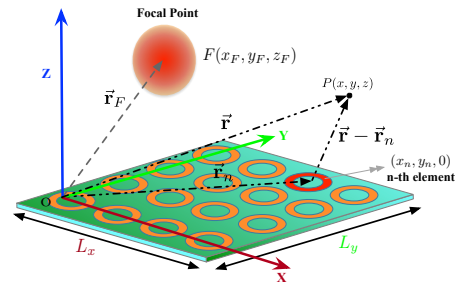


Fig. 12: Magnetic Antenna Array forms a near-field focal point at inventory region. ensure comprehensive coverage, we utilize an array of coil antennas to shape the detection zone as needed. As previously discussed, the near-field range R is influenced by the square of the antenna aperture D , following the relationship $2D^2 / \lambda$. Consequently, augmenting the aperture by a factor of three through an array setup could lead to a ninefold enhancement in the near-field range.

For an antenna array with N coils, as shown in Fig. 12, adjacent coils are spaced by $\lambda/2$. The n^{th} coil's position is represented by \vec{r}_n or coordinates $(x_n, y_n, 0)$ with n spanning from 1 to N . Each coil follows a uniform radiation pattern, denoted as $\hat{B}(\vec{r})$, indicating the magnetic field vector. This pattern is adjusted based on the decay factor $\frac{1}{R} e^{-\mathbf{J}2\pi R / \lambda}$, where R denotes the maximum operational range. The total magnetic field generated by the array at an observation point $P(x, y, z)$ or \vec{r} is given by:

$$B(\vec{r}) = \sum_{n=1}^N C_n B_n(\vec{r}) = \sum_{n=1}^N A_n e^{\mathbf{J}\phi_n} \cdot \hat{B}(\vec{r} - \vec{r}_n) \cdot \frac{e^{-\mathbf{J}2\pi \|\vec{r} - \vec{r}_n\| / \lambda}}{\|\vec{r} - \vec{r}_n\|} \quad (5)$$

where $C_n = A_n e^{\mathbf{J}\phi_n}$ is the n^{th} coil's complex excitation coefficient. Each coil is activated with an amplitude A_n and a modifiable phase ϕ_n .

To direct the magnetic field towards the ROI, the phase shifts of the N coils' excitation coefficients in the array must be tuned. For a desired concentration of the magnetic field at point \vec{r}_F , the distance to the origin is $R_F = \|\vec{r}_F\|$ and the unit vector pointing to this spot is $\hat{r}_F = \vec{r}_F / \|\vec{r}_F\|$. The conjugate phase method, as referenced in [20, 21], suggests setting each antenna's phase ϕ_n as:

$$\phi_n = \frac{2\pi}{\lambda} \|\vec{r}_F - \vec{r}_n\| = \frac{2\pi}{\lambda} \sqrt{R_F^2 + \|\vec{r}_n\|^2 - 2R_F \vec{r}_F \cdot \vec{r}_n} \quad (6)$$

When R_F is much larger than coil size L , the phase adjustments needed to focus on point F are linear and quadratic. The Fresnel approximation, cited in [22], captures this:

$$\varphi_n \approx -\frac{2\pi}{\lambda} (\vec{r}_F \cdot \vec{r}_n) + \frac{2\pi}{\lambda} \frac{\|\vec{r}_n\|^2}{2R_F} \quad (7)$$

A constant phase term, $-2\pi R_F/\lambda$, is omitted as it's relatively insignificant. This approximation is valid with an error under $\pi/8$ if $R_F > \sqrt[3]{L^4/8\lambda}$. However, for closer focal points, necessitating $F \gg L$ to be invalid, Eqn. 6 should be used for accurate phase fine-tuning. To achieve complete coverage of a ROI, the array simply needs to adjust its focal point for meticulous traversal of the area. The small size of the area renders the scanning process effortlessly manageable in practical applications. Furthermore, inventory advancements [9, 23, 24] that prioritize tag localization before communication can be swiftly integrated into RFID+, given its primary focus on enhancing the RF frontend, which permits extensive customization for the signal processing backend.

5 Fast Inventory

In this section, we incorporate the far-field UHF RFID system with the proposed near-field UHF RFID system to expedite inventory processing for tags within the ROI.

5.1 Dual-Coupling Systems

Magnetically-driven RFID systems, despite recent advancements, can only reach a maximum range of about 2.5m, significantly less than the 12m of radiatively-driven RFIDs due to magnetic properties. This constrains their use to smaller ROIs like gates or checkout lanes. Within these narrow confines, a high reading rate, the number of tags recognized per second, becomes essential. Slow readings might miss rapidly moving tags. Fig. 2 shows a self-service checkout scenario, where the system must quickly detect all tagged items in a brief timeframe to ensure a smooth customer experience. Currently, prevalent RFID systems use the Q-adaptive anti-collision protocol, a time-division-based ALOHA derivative. As described in [25], the peak efficiency of such protocols is approximately 36.8%. This means nearly 74% of the time is lost to channel contention, posing a significant efficiency challenge.

To mitigate the low efficiency in the channel competition, we present a prefetching mechanism that harmoniously combines both radiatively-driven RFID and magnetically-driven RFID systems to enhance the reading speed within the ROI. In this configuration, one reader interfaces with a patch antenna, while another is connected to our innovatively designed coil antenna. For clarity, the two readers are called *far-field reader* and *near-field reader*, respectively. Both antennas are strategically positioned toward the direction from which the tags approach. As depicted in Fig. 2(c), a conceivable setup would have the two antennas suspended above the checkout lane, angled antero-inferiorly. This arrangement ensures that the coil antenna encompasses the entirety of the near-field ROI

(approximately the 3m-long lane), while the patch antenna extends its coverage to a broader 10m-long far-field region, inclusive of the ROI and its surrounding area. Leveraging the extended reach of the far-field RFID reader, it becomes feasible to preemptively identify a set of candidate tags expected to traverse through the ROI. While this set might occasionally register cross-readings or omit certain tags, it still offers a substantial advantage by expediting the operations of the near-field reading. In summary, the far-field antenna initially pre-fetch a set of potential tags, enabling the near-field reader to swiftly verify their presence in the ROI based on the far-field's prior knowledge. This time-divided dual-stage approach guarantees that operations in the far-field and near-field do not interfere with each other.

5.2 Acceleration via Perfected Bloom Filter

A Bloom filter (BF) is a space-efficient probabilistic data structure to represent a set of elements. It can be used to fast test whether an element is a member of the set. More introduction about the BF refers to Appendix. C. Initially, the far-field reader collects a set of candidate tags, denoted by T , utilizing the time-consuming Q-adaptive algorithm. The EPCs of these collected tags are then used to construct a Candidate Bloom Filter (BF). Notably, the construction does not necessitate any back-and-forth communication between the reader and the tags, but it is generated by the algorithm. Both the EPCs and the BF are passed to the near-field reader via Ethernet cables.

In the next phase, the near-field reader uses the previously obtained BF to check for the presence of tags within the ROI quickly. Rather than transmitting their full 96-bit EPCs, the tags merely send 16-bit RN_{16} packets to indicate their presence, thus speeding up the inventory process significantly. We adopt the method outlined in previous work [26, 27] to test the BF on-site directly, which has theoretically demonstrated that the acquisition overhead is reduced by approximately 60%. The algorithm subsequently performs a comparative analysis to identify which candidate tags are genuinely in the ROI, i.e., checking the slots during which a desired tag responds based on the hashing results. This can be seen as a streamlined polling algorithm that verifies tags against a predefined list of names without the need for channel competition. Finally, for missing tags that are not indicated by the BF, the near-field reader uses the `Select` command to explore them.

6 Implementation

In this section, we introduce the system implementation of RFID+ and conduct the microbenchmark on coil arrays.

6.1 Fabrication

Given that RFID+ utilizes dual-coupling to blend far-field and near-field characteristics, it necessitates two distinct sets of reader hardware for implementation in actual deployments. Specifically, a commercial Impinj R420 reader [10], accompanied by its patch antenna, serves as the far-field reader in

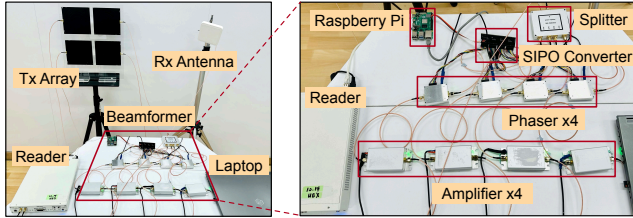


Fig. 13: Experiment setup.

our prototype. In contrast, the near-field reader is custom-constructed around the foundation of the USRP X310 [11].

- Near-Field Reader.** Our near-field reader prototype is anchored in the capabilities of the USRP X310, which boasts two independent RF frontend configurations. One interface is dedicated to an array of coil antennas for transmission (TX). The secondary interface liaises with a compact patch antenna designed for reception (RX). It should be noted that integrating the TX and RX into a monostatic mode is technically feasible and would further reduce the system’s size, benefiting dynamic scenarios. The architectural blueprint of the reader is shown in Appendix D. Upon upconversion in the USRP, the resultant signal is split into four distinct pathways. Each trajectory is orchestrated by an analog phaser (i.e., PHSA-152+ from Mini-Circuits [28]). These phasers enable meticulous phase tuning with an eight-bit granularity. The signals undergo amplification to achieve a cumulative transmission power of 30 dBm before they are broadcasted by the quartet of coil antennas. A Raspberry Pi 4 Model B [29] orchestrates the coordination among the phaser units.

- Coil Array.** At the heart of the system lies a 2×2 coil antenna array, encompassing four distinct coil antennas, each of which has a 75mm radius and about 1.4λ circumference. (see Fig. 10). The exact size and shape of the antenna are determined through iterative optimization to enhance the near-field magnetic intensity. As depicted in Fig. 13, these antennas are integrated onto a two-layer 1.6mm FR-4 printed circuit board (PCB), with HIS reflectors secured to the rear via plastic standoffs. They operate primarily around the 920MHz. Performance enhancement is achieved with an impedance-matching circuit, aligning the antenna to the 50Ω RFID reader standards. Each antenna unit, measuring 17cm by 16cm, incurs an approximate manufacturing expense of \$65.53, as detailed in Appendix E.

6.2 Microbenchmark

Before embarking on a detailed performance evaluation, we initially provide a quantitative analysis of the performance improvements attributable to each antenna design component.

- Component Gain.** We used a magnetic field probe to measure the H-field strength induced by each component of the designed antenna, assessing their respective gains. Different coils, such as conventional single-turn, segmented-line single-turn, multi-turn, along with HIS reflectors, were constructed for evaluation. The data in Tab. 1 show that the gains from the capacitor-segmented, multi-turn, and direc-

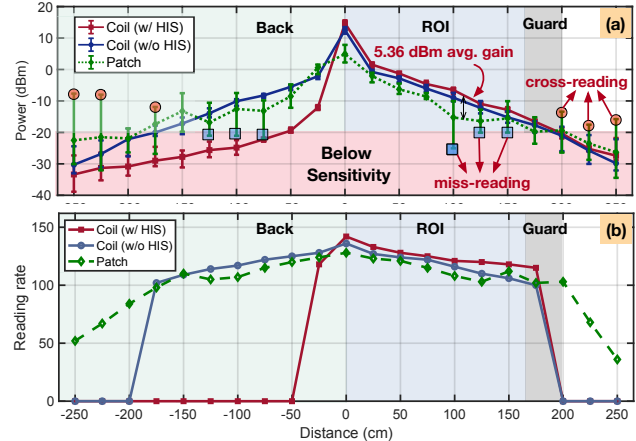


Fig. 14: Controllability Analysis across Different Antennas. (a) and (b) show the signal strength and reading rate as a function of distance, respectively.

tional components were 3.01 dB, 1.96 dB, and 1.68 dB, respectively, contributing to a total increase of 6.65 dB in the H-field’s peak strength.

Next, we characterize the coil array by analyzing the engineered coil antenna’s attributes. We examined three distinct configurations: the novel coil array with and without an HIS, and a traditional electrical patch antenna devoid of a reflector. For experimental purposes, the antenna was positioned on the XOY plane. Here, positive (or negative) distances signify locations either ahead of (or behind) the antenna along Z-axis. Each configuration was subjected to 20 trials. The reader’s transmitting power was consistently maintained at 30dBm.

- Strength Distribution.** We analyzed the magnetic field distribution in radiative regions using a spectrum analyzer [30] coupled with magnetic field probes, as depicted in Fig. 14(a). (1) Frontside: In front of our coil antenna, magnetic strength gradually decreased with little variation. Conversely, the EM field from the patch antenna fluctuated significantly, with strengths ranging from -25 to 11dBm@100cm. Considering a sensitivity threshold of -20dBm [31], the patch antenna could cause miss-readings @100-200cm and potential cross-readings @200-250 cm due to EM field unpredictability. (2) Backside: Behind the coil, the strength quickly fell below the sensitivity level, attributed to null-phase-shift reflections from the HIS. These reflections added an average 1.68dB gain to the frontside magnetic field, equivalent to a 1.5 times power gain. Our findings emphasized the heightened issues of miss-reading and cross-reading in traditional RFID antennas. In contrast, magnetic antennas exhibited enhanced controllability due to reduced multipath propagation effects. This study underscores the superiority of the proposed coil antenna and HIS in spatial control.

- Effective Coverage.** Reading rates, defined as the number of readings recognized per second (r/s), were gathered across a range of -250 to 250 cm. The results are portrayed in Fig. 14(b). Frontside: Within 25-175 cm, the coil antenna con-

Table 1: Each Components’ Impact on H-Field Boost.

Elements	Segmented	Multi-turn	HIS	Total
Gain (dB)	3.01	1.96	1.68	6.65

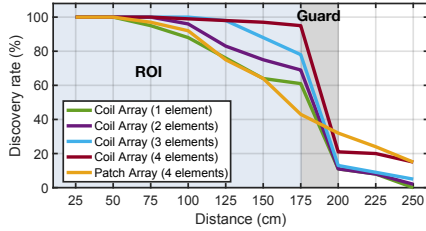


Fig. 15: Inventory Accuracy

sistently showed high reading rates of 115-133 r/s. Beyond 175 cm, this rate drops to zero, mirroring the observed decline in magnetic strength and indicating precise ROI control. Conversely, the patch antenna’s reading capability persists beyond 200 cm, capturing nearly 36 r/s at 250 cm. **Backside:** Beyond -50 cm, the coil antenna w/ HIS reading rate swiftly drops to zero. However, both the coil w/o HIS and the patch antenna display similar reading rates on the backside as seen on the frontside.

Summary. The outcomes of these two experiments emphatically demonstrate the heightened controllability presented by the proposed coil array in both the physical and application dimensions relative to traditional electronic patch antennas. Further, the data suggests a maximum effective range of 175cm plus a 25cm guard zone.

7 Evaluation

In this section, we conduct a group of experiments within a sizable office measuring 50 m² full of multipath reflectors to evaluate RFID+ comprehensively.

7.1 Inventory Accuracy

We conducted a comparative analysis of RFID+ versus conventional RFID systems, centered on inventory accuracy. Both systems employed a 2 × 2 antenna array, with the former utilizing the proposed coil and the latter using a conventional patch antenna. In our test, a dense collection of 100 tags were fixed to a flat surface. The accuracy was measured based on the discovery rate, i.e., the percentage of unique tags identified from the total of 100 tags.

The results are shown in Fig. 15. From the figure, we have two main findings: First, RFID+ boasts near-perfect detection within the ROI, identifying almost all tags for distances up to 175cm. Beyond this zone, the detection drops drastically. Traditional RFIDs maintain a good detection rate only up to 100cm, and their performance diminishes past this point, mostly due to environmental reflections. Second, the number of coils in the array influences detection reach. Distances of flawless detection were reduced to 125cm, 100cm, and 75cm for arrays with 3, 2, and 1 coils, respectively. Overall, RFID+ offers better ROI management than standard RFIDs.

7.2 Inventory Efficiency

We introduce a Bloom Filter-enhanced fast inventory algorithm to expedite the near-field reader’s inventory process as

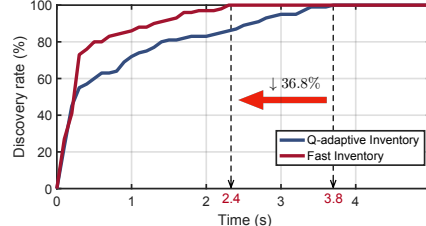


Fig. 16: Inventory Efficiency

discussed in Sec. 5. Leveraging prefetched tags, the far-field reader constructs Bloom Filters to ascertain tags within the ROI swiftly. We compared this approach against conventional inventory methods. Initially, an electronic antenna gathers EPCs from 100 tags, out of which only 30 prefetched and 20 miss-read tags arrived at the near-field ROI. The efficiency is gauged by the discovery rate over time. As illustrated in Fig. 16, our fast inventory approach completes the discovery in 2.4 seconds, contrasted with the 3.8 seconds by the Q-adaptive algorithm. This marks a 36.8% efficiency boost, primarily due to the omission of anti-collision procedure.

7.3 Spatial Controllability

Next, we examine RFID+’s capability in finely tuning the beamforming focal point using the coil array. The focal point represents the peak of energy concentration derived from the coordinated quartet of coils. We directed the system’s focus to five positions along the Z-axis: 40, 60, 80, 100, and 120cm. For each position, a tag was moved from 10cm to 120cm, and the backscattered signal strength was measured.

The findings are illustrated in Fig. 17. As anticipated, signal strength peaked exactly at the 40cm, 60cm, and 80cm marks when directed there. Beamforming focal point increases the average received signal strength (RSS) by approximately 7.73 dB at these locations. However, at 100cm and 120cm, the peaks lagged by 10cm, likely due to power dissipation effects, namely, the combined power from the four coils is unable to compensate for the losses experienced over extended distances. This observation is further mirrored in the peak values decreased with distances, i.e., from -42.3dBm to -46.5dBm, -50.2dBm, -51.5dBm, and -53.7dBm. Such precision in focal adjustments is unparalleled, making it invaluable for specialized scenarios like detecting tags in containers or conveyors.

7.4 Penetrability

We assess the penetration capabilities of RFID+, NFC+ [7], and traditional RFID when tags are positioned on the front (LoS) and backside (NLoS) of various liquid products. Our experiment evaluates six distinct products: M1 (64mm-thick bottled water), M2 (48mm-thick canned Coke), M3 (40mm-thick bottled Coke), M4 (85mm-thick boxed milk), M5 (45mm-thick boxed milk), and M6 (64mm-thick Bottled beer). Such liquid bottles are placed 50cm ahead of the antenna array, which is linked to an Impinj R420 reader used to measure the signal strength.

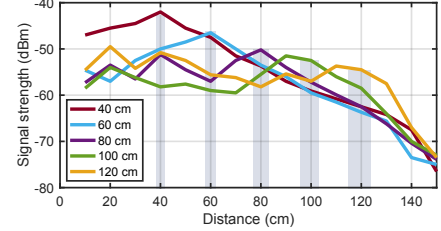


Fig. 17: Spatial Manipulation

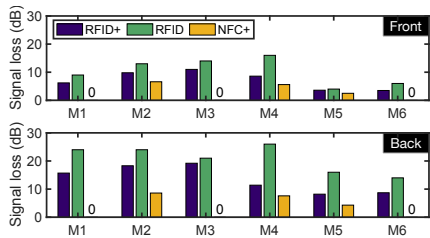


Fig. 18: Penetrability

Fig. 18 illustrates the difference of signal strengths (i.e., loss) acquired when a tag is either affixed to a product or not, respectively. Notably, NFC+, operating at 13.56MHz, exhibits superior performance in most scenarios due to its reduced vulnerability to water interference. Conversely, UHF frequency signals experience higher absorption by water molecules, leading to increased signal loss. Yet, RFID+ surpasses standard RFID systems, registering average losses of 7.1dB and 13.5dB on the product’s front. These losses rise to 13.5dB and 20.8dB for RFID+ and RFID, respectively, on the back. In summary, RFID+ demonstrates potent penetration for liquid products with thicknesses less than 60mm, particularly near the ROI.

7.5 Impact Analysis

Finally, we consider the two potential factors that affect the performance of RFID+.

- Impact of Tag Orientation.** We investigate the role of tag orientation in determining RSS. Three distinct tags, namely Impinj H47, Alien 9662, and NXP U9424 are positioned 50cm from the coil array. These tags are aligned parallel to the XOY, XOZ, and YOZ planes, with the coil array set on the XOY plane. Fig. 19 presents the RSS from the backscatter signals for each tag across the three configurations. Clearly, optimal RSS is achieved when the tag orientation is parallel to the coil array (i.e., XOY), as this allows maximum magnetic flux to traverse the tag’s matching loops. Conversely, the least favorable setup is the YOZ orientation, where minimal flux interacts with the coils. This orientation sensitivity poses a recurring challenge in RFID systems, attributed to the use of planar antennas in tags. A practical workaround involves deploying multiple coils in varied orientations to mitigate such orientation-based discrepancies.

- Impact of Transmission Power.** We investigated the influence of transmission power on the discovery rate, situating tags at intervals between 0.5 m and 1 m from the reader. As depicted in Fig. 20, the discovery rate correlates inversely with decreasing power levels from 32 dBm to 16 dBm. Notably, when transmission power diminishes below 26 dBm, the discovery rate plunges to under 20% for a 1 m distance setting. Moreover, an increased separation between the reader and tags further depresses the rate. For example, at a robust transmission power of 28 dBm, the discovery rate remains optimal at 100% for a 0.5 m distance. Yet, when the distances extend to 0.75 m and 1 m, the rates taper off to 70% and

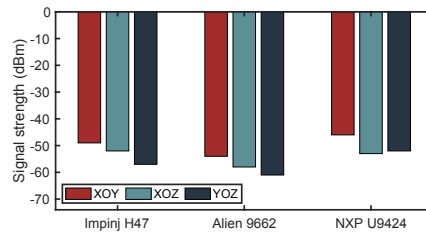


Fig. 19: Impact of tag orientation

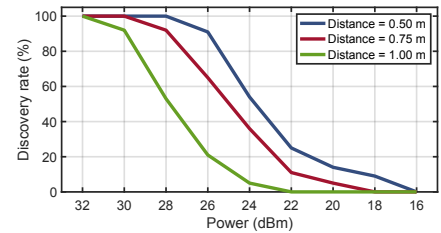


Fig. 20: Impact of transmission power

48%, respectively. This underscores that RFID+, akin to traditional RFID systems, is power-sensitive, primarily because energizing the passive tags consumes a significant portion of the transmitted energy.

8 Pilot Study: Logistic Network Evaluation

8.1 Warehouse Management

We tested RFID+ in a textile factory warehouse with an annual revenue of 100 million USD for contact manufacturing of branded apparel. The factory uses both RFID and barcodes for identification, shown in Fig. 21 (a-c). We set up two 2×2 RFID+ antenna arrays near storage shelves. Over 200 tags were attached to clothing items like T-shirts and jeans, packed in garment boxes, and moved on a Manual Hand Pallet Jack. The number of tags is subject to the Manual Hand Pallet Jack’s maximum capacity and aligns with values reported in earlier studies [8, 12]. As items passed through the scanning zone, RFID+ logged the detected products. Fig. 22 depicts the performance of RFID+, as determined by the mean outcome of ten replicated trials that collectively involved more than 2,000 tags. It detected 98.94% of tags at the gateway, outperforming the commercial radiatively-coupled RFID system’s 77.14%. This is because approximately 10% of the regions are blind spots for reading with conventional radiatively-coupled RFID electrical antennas [4, 32, 33]. When five volunteers, including two students and three workers, manually counted with barcode scanners, the traditional optical barcode identification system noted about 97%. Hence, RFID+ demonstrated superior accuracy against both commercial RFID and manual counts. For cross-reading accuracy, we established a $2m \times 2m$ ROI around the coils/antennas and placed tags randomly at its edges. The results in Fig. 22 show RFID+ had a negligible 0.09% cross-reading rate, significantly less than the UHF RFID system’s 42%. The manual method registered 1.4%, a number potentially increasing with working overtime. In summary, RFID+ excels in minimizing cross-reading and miss-reading when contrasted with both traditional RFID systems and manual inventory methods. It is even capable of approaching the performance of the state-of-the-art (SOTA) system, NFC+ [7], which records a mere 0.03% rate of miss-readings and a zero cross-reading rate for randomly oriented objects. The comparison in Appendix E also highlights RFID+’s out-performance over another SOTA system RFGO [8] in terms of generality, affordability, and ease of deployment.



Fig. 21: Deploying RFID+ in real-world logistics networks. (a-c) show the application in warehouse management, whereas (d-e) illustrate the application in supply chain planning.

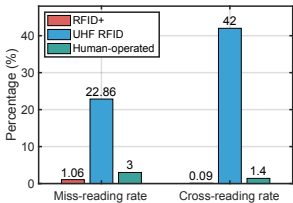


Fig. 22: Performance in Warehouse

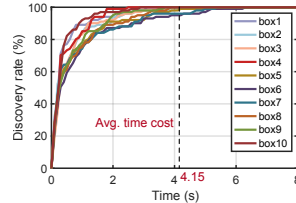


Fig. 23: Performance in Logistics

8.2 Supply Chain Planning

We further explored RFID+’s efficacy in a supply chain setting, wherein boxed products traverse through a conveyor scanning gateway. This conveyor bridges the warehouse and the truck’s cargo hold. We demarcated an inventory zone (i.e., ROI) on the conveyor, dimensions being $1.5 \times 0.5 \times 1.6\text{m}^2$, as visualized in Fig. 21(d-e). Each box, housing around 150-200 garments based on the apparel type, is strategically positioned on the conveyor at 1.5m gaps. Whenever a box enters the designated zone, the conveyor intuitively reduces its speed for inventory purposes. Given the tags’ movement on the conveyor and the minimal interference risk from neighboring tags due to the deliberate spacing, our system consistently showcased flawless performance without any miss-reading or cross-reading instances. Fig. 23 portrays the discovery rate vis-a-vis the time expenditure for ten sequential boxes. An average time consumption of roughly 4.15 seconds is observed for each box. This testing underscores RFID+’s prowess to seamlessly integrate into real-world industrial settings, where UHF RFID consistently sidesteps both miss-reading and cross-reading, all within a reasonable timeframe.

9 Related Work

The related work can be categorized into the following areas:

(1) **UHF RFID Communication.** Over time, UHF RFID systems have been thoroughly tested and understood [5, 7, 12, 34–37]. Their vulnerabilities, including missed readings, are heightened in RF-unfriendly environments [38] or due to multipath issues [5]. Historical attempts at remedying these inaccuracies have explored beamforming [39], nonlinear backscattering [40], wideband signal [12] and wave optimization [41, 42]. Besides missed readings, cross-reading errors are a challenge [43]. Localizing UHF RFID tags has been a primary method to sieve out unwanted tags from the ROI [12, 34]. Still, most localization solutions are antenna-intensive, with RFGo [8] using eleven antennas, proving costly and intricate for industrial settings. The NFC+ solution [7] proposes enhanced NFC technology as a UHF RFID substitute. Although

NFC is highly secure [44], its low throughput is its Achilles’ heel. The industry has explored merging HF NFC and UHF RFID technologies by developing dual-frequency tags [45]. However, this approach compromises the low-cost benefit of standard tags due to the need for custom-designed alternatives. In contrast, RFID+ innovatively combines the best features of both technologies, enabling accurate UHF RFID tag detection with spatially controllable magnetic fields while also ensuring full compatibility with legacy RFID tags.

(2) **Magnetic Antenna Design:** Recent studies have focused on developing magnetic antennas for near-field UHF RFID applications [46, 47], highlighting this technology’s potential to substitute LF/HF RFID in tagging individual items [48]. Traditional solid-line loop antennas primarily be utilized as RFID reader antennas in low frequency [49] and high frequency [50, 51] RFID systems. However, these antennas struggle to maintain a uniform magnetic distribution within the ROI at the UHF band, mainly due to their inability to be electrically small [14]. Addressing this, Dobkin et al. introduced the use of lumped series capacitors in loop antennas to counteract current nulls and enhance magnetic strength in the UHF range [52]. Later studies [15, 17] examined the properties of segmented line capacitors, eliminating the need for discrete circuit components. This led to investigations into various distributed capacitor designs [53–56]. While our work is inspired by existing research, RFID+ is the first to harmoniously integrate disparate elements (e.g., capacitor-segmented loops, multi-turn UHF coils, HISs, coil arrays, etc) into a unified practical system.

10 Conclusion

This work introduces RFID+, a highly accurate and reliable system for RFID tag inventory. RFID+ utilizes the tailored magnetic field to achieve a 99% discovery rate within the ROI, simultaneously preventing cross-reading of tags outside this area. Our warehouse analysis indicates that RFID+ has the potential to revolutionize the logistics industry.

Acknowledgements

We thank all anonymous reviewers and our shepherd Dr. Zerina Kapetanovic for their help and insightful feedback. This work is supported by the NSFC Key Program (No. 61932017), UGC/GRF (No. 15204820, 15215421), Innovation and Technology Fund (ITS/099/21), and Shenzhen Fundamental Research Program (No. JCYJ20230807140410022). Zhenlin An and Lei Yang are co-corresponding authors.

References

- [1] E. C. Jones and C. A. Chung, *RFID in logistics: a practical introduction*. CRC press, 2007.
- [2] Z. Zhang, G. Xu, and E. C. Kan, "Outlooks for uhf rfid-based autonomous retails and factories," *IEEE Journal of Radio Frequency Identification*, 2022.
- [3] S. Pradhan, E. Chai, K. Sundaresan, S. Rangarajan, and L. Qiu, "Konark: A rfid based system for enhancing in-store shopping experience," in *Proceedings of the 4th International on Workshop on Physical Analytics*, 2017, pp. 19–24.
- [4] C. Loo, A. Elsherbeni, F. Yang, and D. Kajfez, "Experimental and simulation investigation of rfid blind spots," *Journal of Electromagnetic Waves and Applications*, vol. 23, no. 5-6, pp. 747–760, 2009.
- [5] M. Taguchi and H. Mizuno, "Analysis of dead zone of rfid system," in *2006 IEEE Antennas and Propagation Society International Symposium*. IEEE, 2006, pp. 4759–4762.
- [6] J. Wang, L. Chang, O. Abari, and S. Keshav, "Are rfid sensing systems ready for the real world?" in *Proc. of ACM MobiSys*, 2019, pp. 366–377.
- [7] R. Zhao, P. Wang, Y. Ma, P. Zhang, H. H. Liu, X. Lin, X. Zhang, C. Xu, and M. Zhang, "Nfc+ breaking nfc networking limits through resonance engineering," in *Proc. of ACM SIGCOMM*, 2020, pp. 694–707.
- [8] C. Bocanegra, M. A. Khojastepour, M. Y. Arslan, E. Chai, S. Rangarajan, and K. R. Chowdhury, "Rfgo: a seamless self-checkout system for apparel stores using rfid," in *Proc. of ACM MobiCom*, 2020.
- [9] Y. Ma, N. Selby, and F. Adib, "Minding the billions: Ultra-wideband localization for deployed rfid tags," in *Proc. of ACM MobiCom*, 2017, pp. 248–260.
- [10] Impinj, "Rain rfid readers, connectivity devices for iot solutions," <https://www.impinj.com/products/readers>, accessed: 2024-02-27.
- [11] Ettus Research, "Usrp x310 high performance software defined radio," <https://www.ettus.com/all-products/x310-kit/>, accessed: 2024-02-27.
- [12] B. Liang, P. Wang, R. Zhao, H. Guo, P. Zhang, J. Guo, S. Zhu, H. H. Liu, X. Zhang, and C. Xu, "Rf-chord: Towards deployable rfid localization system for logistic networks," in *Proc. of USENIX NSDI*, 2023.
- [13] Ansys, "Ansys hfss: 3d high frequency simulation software," <https://www.ansys.com/products/electronics/ansys-hfss>, 2024, accessed: 2024-02-27.
- [14] W. L. Stutzman and G. A. Thiele, *Antenna theory and design*. John Wiley & Sons, 2012.
- [15] Y. Zeng, Z. N. Chen, X. Qing, and J.-M. Jin, "Modeling and characterization of zero-phase-shift lines and optimization of electrically large zpsl loop antennas for near-field systems," *IEEE Transactions on Antennas and Propagation*, vol. 64, no. 11, pp. 4587–4594, 2016.
- [16] A. H. Muqaibel, A. Safaai-Jazi, and S. M. Riad, "Fork-coupled resonators for high-frequency characterization of dielectric substrate materials," *IEEE transactions on instrumentation and measurement*, vol. 55, no. 6, pp. 2216–2220, 2006.
- [17] Z. N. Chen, X. Qing, J. Shi, and Y. Zeng, "Review of zero-phase-shift-line loop antennas for uhf near-field rfid readers," *IEEE journal of radio frequency identification*, vol. 1, no. 4, pp. 245–252, 2017.
- [18] R. Dewan, M. Rahim, M. Hamid, M. Yusoff, N. A. Samsuri, N. Murad, and K. Kamardin, "Artificial magnetic conductor for various antenna applications: An overview," *International Journal of RF and Microwave Computer-Aided Engineering*, vol. 27, no. 6, p. e21105, 2017.
- [19] T. H. Loh, "High impedance surface electromagnetic band gap metamaterials: Design approach and applications for antenna engineering," *Invited Paper*, 2011.
- [20] P. Nepa and A. Buffi, "Near-field-focused microwave antennas: Near-field shaping and implementation." *IEEE Antennas and Propagation Magazine*, vol. 59, no. 3, pp. 42–53, 2017.
- [21] A. Buffi, P. Nepa, and G. Manara, "Design criteria for near-field-focused planar arrays," *IEEE Antennas and Propagation Magazine*, vol. 54, no. 1, pp. 40–50, 2012.
- [22] Wikipedia, "Fresnel diffraction," https://en.wikipedia.org/wiki/Fresnel_diffraction, 2024, accessed: 2024-02-27.
- [23] J. Wang and D. Katabi, "Dude, where's my card? rfid positioning that works with multipath and non-line of sight," in *Proc. of ACM SIGCOMM*, 2013, pp. 51–62.
- [24] L. Yang, Y. Chen, X.-Y. Li, C. Xiao, M. Li, and Y. Liu, "Tagoram: Real-time tracking of mobile rfid tags to high precision using cots devices," in *Proc. of ACM MobiCom*, 2014, pp. 237–248.
- [25] D. Tse and P. Viswanath, *Fundamentals of wireless communication*. Cambridge university press, 2005.
- [26] L. Yang, Q. Lin, C. Duan, and Z. An, "Analog on-tag hashing: Towards selective reading as hash primitives in gen2 rfid systems," in *Proc. of ACM MobiCom*, 2017, pp. 301–314.
- [27] Z. An, Q. Lin, L. Yang, W. Lou, and L. Xie, "Acquiring bloom filters across commercial rfids in physical layer," *IEEE/ACM Transactions on Networking*, vol. 28, no. 4, pp. 1804–1817, 2020.
- [28] Mini-Circuits, "Sphsa-152+ datasheet," <https://www.minicircuits.com/pdfs/SPHSA-152+.pdf>, 2024, accessed: 2024-02-27.
- [29] Raspberry Pi Foundation, "Raspberry pi 4 model b," <https://www.raspberrypi.com/products/raspberry-pi-4-model-b/>, accessed: 2024-02-27.
- [30] Rohde & Schwarz, "Hameg hms3010 3 ghz spectrum analyzer," https://scdn.rohde-schwarz.com/ur/pws/dl_downloads/dl_common_library/dl_brochures_and_datasheets/pdf_1/HAMEG_DB_EN_HMS3000_3010.pdf, accessed: 2024-02-27.
- [31] D. Dobkin, *The rf in RFID: uhf RFID in practice*. Newnes, 2012.
- [32] L. Ukkonen, D. Engels, A. Sydanheimo, and M. Kivikoski, "Reliability of passive rfid of multiple objects using folded microstrip patch-type tag antenna," in *2005 IEEE Antennas and Propagation Society International Symposium*, vol. 2. IEEE, 2005, pp. 341–344.

- [33] R. H. Clarke, D. Twede, J. R. Tazelaar, and K. K. Boyer, "Radio frequency identification (rfid) performance: the effect of tag orientation and package contents," *Packaging Technology and Science: An International Journal*, vol. 19, no. 1, pp. 45–54, 2006.
- [34] Z. Wang, M. Xu, N. Ye, R. Wang, and H. Huang, "Rf-focus: Computer vision-assisted region-of-interest rfid tag recognition and localization in multipath-prevalent environments," in *Proc. of ACM IMWUT*, 2019.
- [35] L. Dodds, N. Naeem, A. Eid, and F. Adib, "Software-controlled polarization for longer-range rfid reading and localization," in *2023 IEEE International Conference on RFID (RFID)*. IEEE, 2023, pp. 90–95.
- [36] L. Dodds, I. Perper, A. Eid, and F. Adib, "A handheld fine-grained rfid localization system with complex-controlled polarization," in *Proc. of ACM MobiCom*, 2023.
- [37] J. Wang, J. Zhang, R. Saha, H. Jin, and S. Kumar, "Pushing the range limits of commercial passive rfids," in *Proc. of USENIX NSDI*, 2019, pp. 301–316.
- [38] Y. Ma, Z. Luo, C. Steiger, G. Traverso, and F. Adib, "Enabling deep-tissue networking for miniature medical devices," in *Proc. of ACM SIGCOMM*, 2018, pp. 417–431.
- [39] S. Chen, S. Zhong, S. Yang, and X. Wang, "A multiantenna rfid reader with blind adaptive beamforming," *IEEE Internet of Things Journal*, vol. 3, no. 6, pp. 986–996, 2016.
- [40] D. Vasisht, G. Zhang, O. Abari, H.-M. Lu, J. Flanz, and D. Katabi, "In-body backscatter communication and localization," in *Proc. of ACM SIGCOMM*, 2018, pp. 132–146.
- [41] Z. An, Q. Lin, Q. Pan, and L. Yang, "Turbocharging deep backscatter through constructive power surges with a single rf source," in *Proc. of IEEE INFOCOM*, 2021.
- [42] S. Sabesan, M. J. Crisp, R. V. Penty, and I. H. White, "Wide area passive uhf rfid system using antenna diversity combined with phase and frequency hopping," *IEEE Transactions on Antennas and Propagation*, vol. 62, no. 2, pp. 878–888, 2013.
- [43] M. Bolic, M. Rostamian, and P. M. Djuric, "Proximity detection with rfid: A step toward the internet of things," *IEEE Pervasive Computing*, vol. 14, no. 2, pp. 70–76, 2015.
- [44] D. Dai, Z. An, Q. Pan, and L. Yang, "Magcode: Nfc-enabled barcodes for nfc-disabled smartphones," in *Proc. of ACM MobiCom*, 2023, pp. 1–14.
- [45] HUAYUAN RFID NFC Manufacturer, "Dual frequency rfid cards," <https://www.huayuansh.com/products/rfid-smart-cards/dual-frequency-rfid-cards/>, 2024, accessed: 2024-02-27.
- [46] B. Shrestha, A. Elsherbeni, and L. Ukkonen, "Uhf rfid reader antenna for near-field and far-field operations," *IEEE Antennas and Wireless Propagation Letters*, vol. 10, pp. 1274–1277, 2011.
- [47] X. Qing, C. Goh, and Z. Chen, "Segmented loop antenna for uhf near-field rfid applications," *Electronics Letters*, vol. 45, no. 17, pp. 872–873, 2009.
- [48] P. V. Nikitin, K. Rao, and S. Lazar, "An overview of near field uhf rfid," in *2007 IEEE international conference on RFID*. IEEE, 2007, pp. 167–174.
- [49] A. Diet, Y. Le Bihan, C. Conessa, F. Alves, M. Grzeskowiak, M. Benamara, G. Lissorgues, M. Biancheri-Astier, and A. Pozzebon, "Lf rfid chequered loop antenna for pebbles on the beach detection," in *2016 46th European Microwave Conference (EuMC)*. IEEE, 2016, pp. 41–44.
- [50] M. Benamara, M. Grzeskowiak, A. Diet, G. Lissorgues, Y. Le Bihan, S. Protat, and C. Conessa, "A twisted loop antenna to enhance hf rfid detection for different tag positioning," in *2016 10th European Conference on Antennas and Propagation (EuCAP)*. IEEE, 2016, pp. 1–5.
- [51] X. Qing, Z. N. Chen, and A. Cai, "Multi-loop antenna for high frequency rfid smart shelf application," in *2007 IEEE Antennas and Propagation Society International Symposium*. IEEE, 2007, pp. 5467–5470.
- [52] D. M. Dobkin, S. M. Weigand, and N. Iyer, "Segmented magnetic antennas for near-field uhf rfid," *Microwave Journal*, vol. 50, no. 6, p. 96, 2007.
- [53] Y. S. Ong, X. Qing, C. K. Goh, and Z. N. Chen, "A segmented loop antenna for uhf near-field rfid," in *2010 IEEE Antennas and Propagation Society International Symposium*. IEEE, 2010, pp. 1–4.
- [54] A. L. Borja, A. Belenguer, J. Cascon, and J. R. Kelly, "A reconfigurable passive uhf reader loop antenna for near-field and far-field rfid applications," *IEEE Antennas and Wireless Propagation Letters*, vol. 11, pp. 580–583, 2012.
- [55] Y. Zeng, X. Qing, Z. N. Chen, and J.-M. Jin, "Directional uhf near-field rfid reader antenna with an improved magnetic field distribution," in *2016 IEEE Region 10 Conference (TENCON)*. IEEE, 2016, pp. 135–137.
- [56] Z. D. Wang, Y. Z. Yin, X. Yang, and J. J. Wu, "Design of a wideband horizontally polarized omnidirectional antenna with mutual coupling method," *IEEE Transactions on Antennas and Propagation*, vol. 63, no. 7, pp. 3311–3316, 2015.
- [57] Mike Lenehan, "Monza 4 datasheet – impinj support portal," <https://support.impinj.com/hc/en-us/articles/202756908-Monza-4-Datasheet>, accessed: 2024-02-27.
- [58] Impinj, "Rain rfid tag chips for the internet of things," <https://www.impinj.com/products/tag-chips>, 2024, accessed: 2024-02-27.
- [59] Alien Technology, "Tags," <https://www.alientechnology.com/products/tags/>, accessed: 2024-02-27.
- [60] NXP Semiconductors, "Ucode rain rfid uhf," https://www.nxp.com/products/rfid-nfc/ucode-rain-rfid-uhf:MC_50483, 2023, accessed: 2024-02-27.
- [61] Laxcen, "RFID," <http://www.laxcen.com/rfid.html>, 2023, accessed: 2024-02-27.
- [62] Z. An, Q. Lin, L. Yang, and W. Lou, "Embracing tag collisions: Acquiring bloom filters across rfids in physical layer," in *Proc. of IEEE INFOCOM*, 2019, pp. 1531–1539.
- [63] B. Sheng, Q. Li, and W. Mao, "Efficient continuous scanning in rfid systems," in *Proc. of IEEE INFOCOM*, 2010.
- [64] L. Xie, Q. Li, X. Chen, S. Lu, and D. Chen, "Continuous scanning with mobile reader in rfid systems: An experimental study," in *Proc. of ACM MobiHoc*, 2013, pp. 11–20.

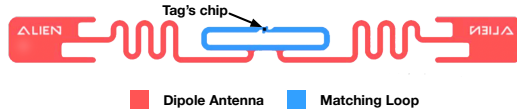


Fig. 24: Structure of a Typical UHF RFID Tag. It consists of an integrated chip, matching loop and a dipole antenna.

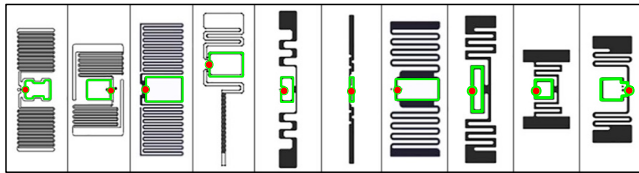


Fig. 25: The Popular UHF RFIDs. Each type of tag contains a matching loop (green) that bridges the dipole antenna with the chip.

Appendix

A Magnetically-driven UHF RFID Systems

Without loss of generality, Fig. 24 displays a standard UHF RFID tag design, showcasing a small loop (highlighted in blue) adjacent to its chip. Consistently, as Fig. 25 further demonstrates, it is a fundamental trait for nearly every RFID tag to embody a single-turn coil, known as the matching loop. This loop is instrumental in the magnetic energy harvesting process within our system. To inventory such tags, the reader must adhere to the UHF RFID Gen2 air interface protocol, which involves several steps: (1) The process begins with the reader initiating an inventory session by sending out a *Select* command to select a group of tags for participation. (2) This is followed by a *Query* command to initiate a new frame, during which each tag that has not yet been identified chooses a random time slot to respond. (3) In its allocated slot, a tag first sends out a 22-bit short response (i.e., RN16) to aid in detecting signal collisions. (4) If the RN16 is successfully decoded by the reader, it indicates a collision-free transmission from a single tag (known as a singleton slot). (5) Subsequently, the reader requests a longer, 128-bit response (i.e., EPC) by issuing an *ACK* command. Thus, a tag is required to first transmit an RN16 response before it can send its full EPC response.

Inventory with the Coil Antenna. To test the viability of a magnetically-driven UHF RFID system, we initiated a preliminary experiment using the configuration depicted in Fig. 5. An Impinj M4 tag [57] was placed 10cm away as part of the experimental setup. *The Impinj reader is equipped with the coil antenna for tag activation and querying.* Concurrently, the sniffer discreetly recorded the leaked RF transmissions. As depicted in Fig. 26, the normalized amplitude of the intercepted signal is showcased. The figure clearly delineates the reader’s command signals and the tag’s backscattered responses. The inventory process kicks off with a *Select* command, promptly followed by a *Query*. Responding to the query, the tag emits a RN16 reply that includes a fixed 6-bit preamble for signal identification, succeeded by 16 random bits to facilitate channel contention, as illustrated in Fig. 6.

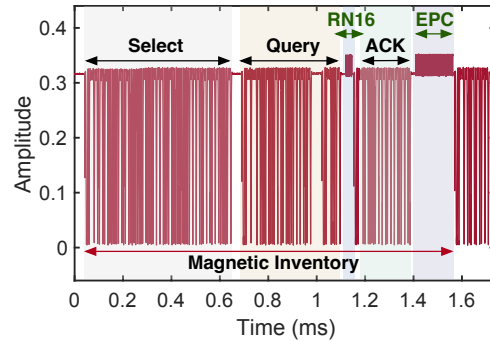


Fig. 26: RF signal acquired by the sniffer when the tag was queried by a magnetically-driven UHF RFID reader.

This is subsequently acknowledged by the *ACK* command, indicating the slot’s availability. Conclusively, the tag broadcasts its EPC. This process closely parallels the inventory sequence observed in radiatively-coupled RFID Gen2 systems. It validates that COTS RFID tags can be activated and queried using magnetic fields while the communication protocol remains consistent.

Versatility Validation. To underscore the versatility of the magnetically-driven approach, we further tested ten tags from leading manufacturers such as Impinj [58], Alien [59], NXP [60], and Laxcen [61]. Every tag is placed 50cm in front of RFID+ to assess its readability. Their performance is reflected in reading rates, outlined in Table. 2. Reading rates ranged from 105 to 129, with Impinj’s H47 tag outperforming the rest and Alien’s 9654 tag at the lower end. These differences are likely due to variations in the tags’ internal loop structures. Broadly speaking, tags with larger loop diameters tend to register a heightened coupling coefficient, leading to better reading rates. However, every tag was effectively recognized by the magnetically driven reader, highlighting the universal efficacy of our magnetically-driven RFID solution.

B High-Impedance Surface

Fig. 27 showcases the simulated results of the HIS reflector, utilizing Ansys HFSS [13] as the simulation platform. Throughout the simulation process, the spiral antenna was strategically positioned a mere 10 mm ($\ll \lambda/4$) above the HIS substrate. In the absence of the reflector, as visualized in Fig. 27(a), the magnetic field displays a balanced distribution across both the superior and inferior facets of the an-

Table 2: The configuration and reading rate of different tags

Tag(#)	MFR.	IC	Model	Size(mm ²)	Reading rate (t/s)
T1	Impinj	Monza 4QT	H47	50 × 50	129
T2		Monza R6	ER62	74 × 18	119
T3	Alien	Higgs 3	9662	70 × 17	121
T4		Higgs 3	9640	94.8 × 8.25	126
T5		Higgs 3	9654	93 × 19	105
T6		Higgs 3	9962	73.5 × 20.2	117
T7	NXP	Ucode8	U9624	98 × 27	105
T8		UR108	U7015	70 × 15	126
T9	Laxcen	Monza 4QT	C90G	90 × 20	107
T10		Monza 5	C50D	50 × 30	106

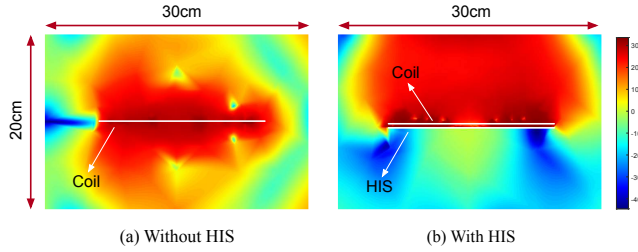


Fig. 27: Simulated magnetic intensity without and with an HIS reflector attached to the spiral coil antenna. (a) shows the magnetic field distribution on the antenna’s tangent radiation plane without HIS; (b) illustrates the magnetic field distribution with the HIS in place.

tenna. Yet, when the reflector is introduced beneath the UHF magnetic antenna, as illustrated in Fig. 27(b), there is a pronounced intensification of the field on the antenna’s top surface, accompanied by a significant attenuation on its lower side. These results vividly demonstrate the prowess of the HIS-based reflector in steering the magnetic field, accentuating the radiation efficiency and gain in the desired direction while simultaneously attenuating undesired emissions. The incorporation of this reflector could lead to power conservation for the antenna due to its innate ability to enhance signal superposition constructively.

C Fundamentals of Bloom Filter

Utilizing a set of prefetched tags (i.e., candidate tags), there is no longer a need for exhaustive inventory processing in the near-field. Instead, we employ Bloom filters (BF) to swiftly ascertain the presence or absence of these candidate tags in the region of interest [26, 62–64]. BF is a time-efficient probabilistic data structure that accurately represents the existing set of tags. As depicted in Fig. 28, a Bloom filter succinctly characterizes a set $T = \{t_1, t_2, \dots, t_n\}$ comprising n tags through an array of M bits, which are initialized to 0. By leveraging K distinct hash functions, denoted as $\{h_1, h_2, \dots, h_K\}$, each tag is mapped to an integer within the span of $\{1, \dots, M\}$. For every tag t in T , the bits corresponding to $H = \{h_1(t), \dots, h_K(t)\}$ are assigned the value 1. Even though a bit might encounter collisions, its value remains 1. To determine if a tag t resides in T , it suffices to verify whether all bits associated with $\{h_1(t), \dots, h_K(t)\}$ are indeed 1. If even one isn’t, then t is not a member of the set. As a case in point, tag t_2 is not part of T as, in the test BF, its seventh bit does not hold the value of 1. If all related bits are 1, we postulate that t is within T , albeit with a caveat: there is a minuscule chance (e.g., < 0.001) of misclassification, leading to a false positive. Moreover, if a particular bit is 0 in the candidate BF but transitions to 1 in the test BF, this alteration indicates the presence of a previously unaccounted-for tag in the ROI. For example, the last bit ‘1’ in the test BF is caused by the uncollected tag t_{n+1} (i.e., $t_{n+1} \notin T$).

Time Efficiency. In less complex situations (e.g., $n < 100$), using a dictionary search method suffices to meet the goals, specifically enabling the system to expedite the inventory

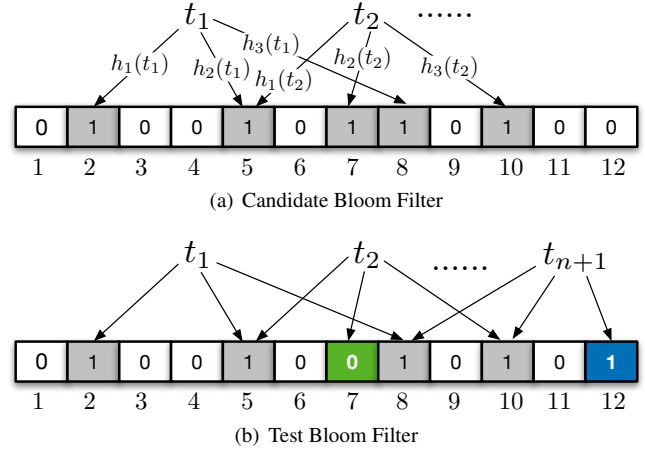


Fig. 28: Fast Inventory with Bloom Filters. (a) shows a candidate Bloom filter, which is a concise bitmap representing the collected candidate tags, acquired by the far-field reader. (b) shows the test Bloom filter acquired from the near-field reader on site. By comparing these two bitmaps, we can swiftly discern the tags residing within the ROI. For example, the tag t_2 is a cross-reading, i.e., absent from the ROI, while tag t_{n+1} represents a tag undetected by the far-field reader.

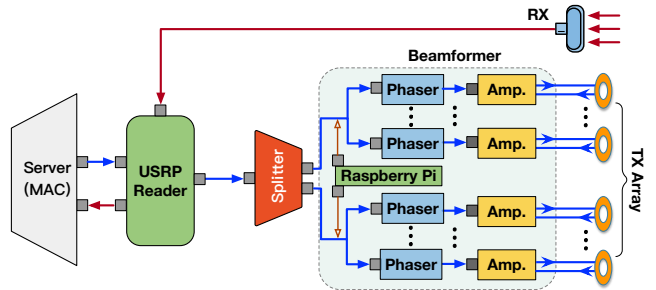


Fig. 29: Illustration of Near-Field Reader

process through straightforward dictionary queries. However, with the increase in the number of tags, the search time complexity of a dictionary scales linearly as $O(n)$. On the other hand, BFs offer efficient lookups for tag presence, maintaining fast query times regardless of the dataset’s size n , with a complexity of $O(\log_2(n))$. Therefore, BF is ideally suited for rapid inventory applications in warehouses.

D Architecture of Near-Field Reader

The detailed architecture of the near-field reader is illustrated in Fig. 29. After undergoing upconversion in the USRP, the emergent signal is bifurcated, creating four separate paths. These distinct routes are meticulously controlled by analog phasers, specifically the PHSA-152+ model from Mini-Circuits [28]. These state-of-the-art phasers grant a high level of precision in phase adjustments, offering an impressive eight-bit granularity. Following this, the signals are subjected to an amplification process, ensuring they achieve a robust transmission power of 30 dBm. Subsequently, these fortified signals are disseminated by an ensemble of four coil antennas. To streamline and synchronize the operations of the phaser units, a Raspberry Pi 4 Model B [29] is strategically deployed, acting as the central coordination hub with the aid of a cus-

tomized Serial-In to Parallel-Out (SIPO) Converter.

E Compared with Related Systems

In a parallel comparison, RFID+ outperforms the state-of-the-art RFID inventory solution RFGo [8] with respect to generality, cost, and deployment ease: First, RFID+ enables seamless plug-and-play functionality in dynamic environments without the extensive data collection and training RFGo requires. Moreover, RFID+ proves to be more budget-friendly, employing a limited number of lower-cost hardware components like magnetic coils, phase shifters, and HIS reflectors (see

cost breakdown in Tab. 3), in contrast to RFGo’s intricate setup involving 11 USRP X310 units and numerous antennas. Lastly, setting up RFID+ is straightforward, requiring only two perpendicular surfaces, unlike RFGo’s complex three-dimensional antenna configuration.

Table 3: Pricing Estimation for BOM List of One Antenna Unit

Item (#)	Component	Description	Quantity	Price (\$)
1	Coil Antenna	Two-layer PCB	1	5.42
2	HIS Reflector	Two-layer PCB	1	3.06
3	RF Amplifier	SKY65111-348LF	1	2.64
4	Phase Shifter	SPHSA-152+	1	50.41
5	Micro Controller	Raspberry Pi Pico	1	4.00
Total Cost				65.53